Chemical Science

ROYAL SOCIETY OF CHEMISTRY

EDGE ARTICLE

View Article Online
View Journal | View Issue

Cite this: *Chem. Sci.*, 2025, **16**, 6366

All publication charges for this article have been paid for by the Royal Society of Chemistry

Unraveling the effect of alkali cations on Fe single atom catalysts with high coordination numbers†

Yecheng Li,‡[a] Songjie Meng,‡[b] Zihong Wang,[c] Hehe Zhang,[d] Xin Zhao,[c] Qingshun Nian,[c] Digen Ruan,[c] Lianfeng Zou,*[d] Zhansheng Lu *[be] and Xiaodi Ren *[ac]

Received 22nd January 2025
Accepted 7th March 2025

DOI: 10.1039/d5sc00581g

rsc.li/chemical-science

Fe single atom catalysts (SACs) with high coordination numbers have emerged as high-performance catalysts for the conversion of CO_2 to CO. However, the influence of alkali cations at the catalyst–electrolyte interface has not yet been understood clearly. Here, we investigate the role of various alkali metal cations (Na^+, K^+, Rb^+) in catalytic CO_2 reduction reaction (CO_2RR) behavior on high coordination number Fe SACs (FeN_5 and FeN_6) obtained from a facile hard template method. We find that larger cations can greatly promote the CO_2RR and such effects are enhanced with increasing cation concentration. Nevertheless, the hydrogen evolution side reaction (HER) on co-existing N heteroatom sites will be worsened. This trade-off highlights the importance of manipulating the reactive sites for SACs. From theoretical simulation and *in situ* spectroscopy results, we confirm that the functioning mechanism of cations on Fe SACs lies in the enhancement of the adsorption of key intermediates through direct coordination and indirect hydrogen bonding effects. With the rationally designed Fe SACs (FeN_5) and the electrolyte conditions (1 M KOH), our flow cell test demonstrates a maximum Faraday efficiency of CO (FE_{CO}) of approximately 100% at 100 mA cm^{-2}. This research provides significant insights for future SACs and electrolyte design.

1. Introduction

Carbon dioxide (CO_2) is the primary greenhouse gas responsible for global warming, and there is an urgent need to develop technologies that can utilize CO_2. Electrochemical reduction of CO_2 is a promising approach to convert CO_2 into value-added chemicals such as CO,[1,2] HCOOH,[3,4] CH_4,[5,6] C_2H_4,[7–9] and C_2H_5OH.[10,11] Among these products, CO is an important industrial raw material for the Fischer–Tropsch reaction. However, the chemical inertness of CO_2 makes the CO_2-to-CO reaction challenging.[12] To address this issue, researchers have focused on developing various catalyst design strategies to promote the CO_2 reduction reaction (CO_2RR) to improve the reaction activity and selectivity.[13]

Recently, increasing attention has been paid to the electrolyte effect at the catalyst–electrolyte interface. In most cases, the CO_2RR takes place at the gas–liquid–solid three-phase boundary, and thus the electrolyte environment is a pivotal factor affecting the CO_2RR process.[14] Previously, researchers have revealed the effect of different electrolytes on metal catalysts for the CO_2RR. Significant impacts of ionic species and their concentrations in the electrolyte on the faradaic efficiency (FE) and current density (j) have been observed on Au,[15] Ag,[16] and Cu catalysts.[17] However, to our knowledge, there is very scarce research concerning the interaction between single atom catalyst (SACs) and electrolytes. Take Fe SACs as an example, which is a promising catalyst for the CO_2-to-CO conversion with maximum atom utilization and high catalytic activity.[18–21] Ana *et al.* found that pH has no apparent effect on the J_{CO} of Fe–N–C, but significantly enhances J_{H_2} at lower pH.[22] Li *et al.* observed a volcano trend for J_{CO} at Fe-NS-C with increasing electrolyte concentration in the high overpotential region.[23] However, the underlying mechanism of the electrolyte effect on the performance of Fe SACs remains elusive. Recently, enhanced CO_2RR performance of Fe SACs with high coordination numbers has drawn great interest as a result of the changes of the active site symmetric and electronic structure.[24,25] This raises an open question regarding how the electrolyte would interact with such

[a]*Hefei National Laboratory for Physical Sciences at the Microscale, CAS Key Laboratory of Materials for Energy Conversion, University of Science and Technology of China, Anhui 230026, China. E-mail: xdren@ustc.edu.cn*

[b]*School of Physics, Henan Normal University, Xinxiang 453007, China*

[c]*School of Chemistry and Materials Science, University of Science and Technology of China, Anhui 230026, China*

[d]*Clean Nano Energy Center, State Key Laboratory of Metastable Material Science and Technology, Yanshan University, Qinhuangdao, 066004, China. E-mail: zoulf@ysu.edu.cn*

[e]*College of Mathematics and Physics, Beijing University of Chemical Technology, Beijing 100029, China. E-mail: zslu@buct.edu.cn*

† Electronic supplementary information (ESI) available. See DOI: https://doi.org/10.1039/d5sc00581g

‡ Y. L. and S. M. contributed equally.

SACs with high coordination numbers during the CO_2RR. As a result, it is imperative to understand the functioning mechanism of the electrolyte, especially the cation, to guide future system design and industrial application of SACs.

Herein, we develop a facile hard template method to synthesize two different Fe SACs with high coordination numbers, FeN_6 and FeN_5. For both Fe SACs, increasing J_{CO} was observed with a higher cation radius. However, in contrast to traditional metal catalysts, HER side reactions also aggravated when the cation radius increased, which could explain the irregular change of the FE for CO conversion with different cations. Apart from the cation, increasing the ionic concentration enhances the FE_{CO} at Fe SACs at low overpotentials but shows the opposite effect at high overpotentials. However, the J_{CO} of FeN_6 shows a volcano trend at high overpotentials, which is attributed to the significantly enhanced HER due to the abundance of heteroatom sites with high HER activity and the relatively low CO_2RR activity of the Fe–N_6 site, as confirmed by the thiocyanate poisoning test. In contrast, FeN_5 can achieve higher J_{CO} at high overpotentials with the selective removal of HER sites and the promoted formation of Fe–N_5 sites with high CO_2RR activity. The density functional theory in classical explicit solvent (DFT-CES) simulation and *in situ* synchrotron radiation Fourier transform infrared (SR-FTIR) results indicate that cations can coordinate with $*CO_2$ or *COOH intermediates and enhance their hydrogen bonding with H_2O, thus lowering the reaction barrier and facilitating the subsequent charge transfer rate. Further tests of the FeN_5 SACs in the flow cell system demonstrate high selectivity ($FE_{CO} \approx 100\%$ at 100 mA cm^{-2}) in 1 M KOH. This work provides fundamental understandings of the interaction between SACs and electrolytes and guidance for the future design of SACs.

2. Experimental

2.1 Materials

Silica fumed powder (SiO_2, S5130) was purchased from Sigma-Aldrich Co. Ltd. 3,8-Dibromo-1,10-phenanthroline ($C_{12}H_6Br_2N_2$, 97%) was purchased from Bidepharm Co. Ltd. Sodium bicarbonate ($NaHCO_3$, ≥99.5%), tetrahydrofuran (THF, 99.5%), sulfuric acid (H_2SO_4, AR) and ethanol (C_2H_5OH, ≥99.7%) were bought from Sinopharm Chemical Reagent Co. Ltd. Potassium bicarbonate ($KHCO_3$, 99.5%), rubidium bicarbonate ($RbHCO_3$, 99%), rubidium sulfate (Rb_2SO_4, 99%), potassium sulfate (K_2SO_4, 99%), sodium hydroxide (NaOH, 99%) and ferric nitrate nonahydrate ($Fe(NO_3)_3 \cdot 9H_2O$, 99.9%) were obtained from Macklin Co. Ltd. Sodium perchlorate ($NaClO_4$, 99%) was purchased from Aladdin Co. Ltd. All chemicals were used as received without further purification.

2.2 Synthesis of the FeN_6 SAC

The single-atom catalyst was synthesized by a simple hard template method. In a typical synthesis, 1 g SiO_2, 1 g $C_{12}H_6Br_2N_2$ and 0.7 g $Fe(NO_3)_3 \cdot 9H_2O$ were first dissolved in 60 mL THF and stirred for 4 h. Then, the solvent was removed by rotary evaporation. Subsequently, the obtained brown powder was pyrolyzed under flowing N_2 for 2 h at 800 °C. After that, the product was immersed in 2 M NaOH for 2–3 days to remove the template and then was leached in 0.5 M H_2SO_4 at 90 °C for 4 h to remove unstable metallic species. The catalyst was washed with DI water until pH = 7 and collected by centrifugation. Finally, by vacuum drying at 70 °C overnight, the FeN_6 SAC was obtained.

2.3 Synthesis of the FeN_5 SAC

The FeN_5 was obtained by H_2 treatment of FeN_6. The FeN_6 SAC was further pyrolyzed under flowing H_2/Ar = 5% for 1 hour at 800 °C to remove undesired pyrrolic N and pyridinic N. After H_2 treatment, the FeN_5 SAC was successfully obtained.

2.4 Characterization

The X-ray diffraction pattern (XRD) was obtained through a Japan Rigaku Miniflex 600 using Cu Kα radiation (1.54 Å). Raman scattering spectra were recorded with a Renishaw System 2000 spectrometer. N_2 adsorption/desorption analysis were carried out at 77 K using the Micromeritics ASAP 2020 system. Scanning electron microscopy (SEM) observations were carried out on a Gemini SEM 450. Transmission electron microscopy (TEM), Energy dispersive X-ray (EDX) mapping, high-angle annular dark-field scanning transmission electron microscopy (HADDF-STEM) and Aberration-corrected (AC) HAADF-STEM images were acquired on a ThermoFisher Themis. An inductively coupled plasma atomic emission spectrometer (ICP-AES) was employed to quantify the content of Fe using a Thermo scientific iCAP 7400 series instrument. X-ray photoelectron spectroscopy (XPS) measurements were performed using an ESCALAB 250Xi high-performance electron spectrometer. The X-ray absorption spectra (XAS) including X-ray absorption near-edge structure (XANES) and extended X-ray absorption fine structure (EXAFS) of the samples were collected at the Singapore Synchrotron Light Source (SSLS) center, where a pair of channel-cut Si (111) crystals was used in the monochromator. The Fe K-edge XANES data were recorded in a transmission mode. Fe foil was used as the reference. The storage ring was working at the energy of 2.5 GeV with an average electron current of below 200 mA. The acquired EXAFS data were extracted and processed according to the standard procedures using the Athena module implemented in the IFEFFIT software packages.

The *in situ* Specular Reflection Fourier Transform Infrared (SR-FTIR) measurements were recorded between 600 and 4000 cm^{-1} at the Infrared Spectroscopy and Microspectroscopy Endstation (BL01B) in the National Synchrotron Radiation Laboratory (NSRL) in Hefei, China (Fig. S29†). This end station was equipped with an FTIR spectrometer (Bruker 66 v/s) with a KBr beam-splitter and various detectors (here a liquid nitrogen cooled mercury cadmium telluride detector was used) coupled with an infrared microscope (Bruker Hyperion 3000) with a ×16 objective, and can provide infrared spectroscopy measurement with a high spectral resolution of 0.25 cm^{-1}. Each infrared absorption spectrum was acquired by averaging 128 scans at a resolution of 4 cm^{-1}. The CO_2 saturated electrolyte

was selected as the flowing electrolyte and pumped into an electrochemical *in situ* IR cell (Beijing Scistar Technology Co., Ltd) with a flow rate of 2 mL min^{-1}. To guarantee CO_2 saturated the electrolyte, we purged CO_2 in each electrolyte over 10 minutes before the test. The conductive tape was used to gum the catalyst on the glassy carbon electrode to fabricate the working electrode. There was less electrolyte between the electrode and ZnSe window, containing active species adsorbed on the catalyst. All infrared spectral acquisitions were carried out after a constant potential was applied to the working electrode for 10 min. The background spectrum of the working electrode was acquired at an open-circuit voltage before each systemic CO_2RR measurement (Fig. S30a†), and the measured potential ranges of the CO_2RR were −1.0 to −1.6 V *vs.* Ag/AgCl.

2.5 Electrochemical CO_2 reduction experiment

Different electrolytes (see pH in Table S6†) were prepared by bubbling CO_2 into different carbonate and bicarbonate aqueous solutions over 30 minutes. The H-type cell (Fig. S10†) was used as the equipment for CO_2 electrochemical reduction. A Nafion 117 membrane was inserted between the cathodic chamber and anodic chamber. A gas mass flow controller was used to set the CO_2 flow rate at 30 sccm. The Pt sheet and Ag/AgCl were used as the counter electrode and reference electrode, respectively. The working electrode was prepared by the following method: first, 10 mg of the as-synthesized catalyst, 950 μL ethanol, and 50 μL Nafion 117 solution were mixed and sonicated for above 30 minutes to form a homogeneous ink. Next, 100 μL ink was coated on each side of carbon paper (the total area of paper is 1 × 1 cm^2) to ensure a loading of 1 mg cm^{-2}. Last, this electrode was dried in an oven overnight for next use. Before all electrochemical measurement, the working electrode was activated by 100 cycles of cyclic voltammetry (CV) test from −0.6 V to −2.0 V (*vs.* Ag/AgCl). The LSV curves were conducted with the CHI760E electrochemical workstation with a scan rate of 5 mV s^{-1}. The potentials *vs.* the reversible hydrogen electrode (RHE) were measured by transforming the recorded potentials against Ag/AgCl in this work using the following equation:

$$E_{RHE} = E_{Ag/AgCl} + 0.204 + 0.059 \times pH$$

The chronoamperometry tests were conducted at each potential for 10 min (Fig. S14†). The gas products of electrolysis were detected on the FULI GC9702 plus gas chromatograph. High purity helium (99.9999%) was used as the carrier gas for the chromatography. The liquid products of electrolysis were analyzed using a Bruker Avance III HD 400 NMR. The Faraday efficiency (FE) of gas products was calculated by the equation:

$$FE_{CO} = \frac{96\,485\ (C\ mol^{-1}) \times V\ (mL\ min^{-1}) \times 10\ (min) \times n \times A}{158\,728.694 \times 10^9 \times C\ (C)}$$

$$FE_{H_2} = \frac{96\,485\ (C\ mol^{-1}) \times V\ (mL\ min^{-1}) \times 10\ (min) \times n \times A}{0.02404 \times 60 \times 10^{12} \times C\ (C)}$$

V (mL min^{-1}) = gas flow rate measured by a flow meter at the exit of the cell at room temperature and under ambient pressure. n = total number of electrons transferred in the reaction, CO and H_2 are 2. A = volume concentration of CO and H_2 in the exhaust gas from the electrolyzer (GC data). C = the total electricity consumed by the reaction.

Both CO_2RR and HER make contribution for the current in the aqueous electrolyte. The reduction products are detected by gas chromatography and nuclear magnetic resonance for the calculation of FE to accurately evaluate the CO_2RR activity. No liquid products are detected after electrolysis (Fig. S11†). CO is detected from the flame ionization detector (FID) and H_2 is detected from the thermal conductivity detector (TCD). In order to distinguish the contribution of the CO_2RR and HER in current, the partial current density was calculated by the equation:

$$J_{CO} = J_{total} \times FE_{CO}$$

$$J_{H_2} = J_{total} \times FE_{H_2}$$

J_{total} = current density measured by chronoamperometry at different potentials.

For experiments in flow cells, the electrode was prepared by hand-painting the catalyst ink onto the gas diffusion layer (GDL). 10 mg of the FeN_5 catalyst, 50 μL of Nafion, and 950 μL of ethanol were mixed with ultrasound. The 400 μL ink was air-brushed on the GDL (the total area of paper is 2 × 2 cm^2) to ensure a loading of 1 mg cm^{-2}. The prepared gas diffusion electrode (GDE) and Pt foam were used as the cathode and anode, respectively. Their chambers were filled with 1 M KOH. A cation exchange membrane (Nafion 117 membrane) was used to separate the cathode and anode. During the measurements, KOH electrolyte flow was kept constant at 20 mL min^{-1}, and CO_2 gas with a flow rate of 50 sccm was directly fed to the cathode GDL. In order to ensure the experiments to be more accurate, a mass flowmeter was used to monitor the export flow rate.

2.6 DFT calculation

Density functional theory (DFT) computational simulation was performed with the Vienna *ab initio* simulation package (VASP). The generalized gradient approximation (GGA) within the Perdew–Burke–Ernzerhof (PBE) exchange-correlation functional was used in the calculations.[26,27] A vacuum layer of 15 Å was used to avoid periodic image interaction in the z direction, and a kinetic energy cut-off of 500 eV was chosen. A 5 × 5 graphene supercell was used for simulation, and the surface Brillouin zone was sampled using a 3 × 3 × 1 Monkhorst–Pack k point grid. The force convergence criteria and energy convergence criteria were set at 10^{-5} eV, and the convergence threshold was set at 0.02 eV $Å^{-1}$, respectively. In addition, we also considered adding 25 H_2O molecules (density of ∼1 g cm^{-3}) to the subsequent liquid environment for simulation.[28,29]

The formation energy (E_{for}) can be used to characterize the stability of the substrate, the formula is: $E_{for} = E_{total} - E_{slab} - E_{FeN_{5/6}}$, where E_{total}, E_{slab}, and $E_{FeN_{5/6}}$ are the total energy of the

catalyst, graphene slab and $FeN_{5/6}$ molecules respectively. Meanwhile, for the strength of molecular adsorption, adsorption energy (E_a) is defined as: $E_a = E_{X/sub} - E_{sub} - E_X$, where E_{total}, E_{sub}, and E_X are the total energy of the adsorbent, substrate and molecules respectively. According to this definition, the more negative the adsorption energy, the stronger the adsorption.

The reaction processes of reducing CO_2 to CO are calculated as follows:

$$* + CO_2 \rightarrow *CO_2$$

$$*CO_2 + H^+ + e^- \rightarrow *COOH$$

$$*COOH + H^+ + e^- \rightarrow *CO + H_2O$$

$$*CO \rightarrow CO + *$$

The Gibbs free energy for the CO_2RR process is calculated as: $\Delta G = \Delta E - T\Delta S + \Delta ZPE$, where ΔE is the total optimal energy of DFT, ΔS is the entropy difference between the gas phase and adsorption state, ΔZPE corresponds to the zero-point energy, and T is = 298.15 K.

3. Results and discussion

3.1 Synthesis and characterization of Fe single atom catalysts

Because the asymmetric electronic structure of the active site in the high coordination number Fe SACs is beneficial for the CO_2RR compared with FeN_4, we synthesized mesoporous FeN_6 using a simple hard template method (Fig. 1a, see details in the ESI†). Since the *o*-phenanthroline can form a six-coordinate structure with Fe^{3+}, 3,8-dibromo-1,10-phenanthroline was used as the nitrogen source. A silica template was used to obtain a mesoporous structure, which in turn facilitates the contact between the catalyst and the electrolyte. In order to systematically study the electrolyte effect on high-coordination Fe SACs, FeN_5 was also synthesized from FeN_6 by hydrogen treatment. Their structures could be confirmed by various characterization methods. The X-ray diffraction (XRD) pattern (Fig. S2a and S4a†) shows two main peaks at 25° and 42°, corresponding to the (002) and (100) planes of the graphitic carbon, which are also confirmed by the Raman result (Fig. S2b and S4b†). No other obvious peaks can be observed, indicating no iron particles exist after the acid treatment. Fig. S2c and S4c† show the nitrogen adsorption/desorption curves representing the IUPAC IV type, and the pore size distribution map (Fig. S2d, S4d and Table S1†) indicates that that the mean pore sizes of the two samples are around 8 nm. Scanning and transmission electron microscopy (SEM and TEM) images further confirm the mesoporous structure (Fig. 1b, S1a, b and S3a, b†) of the materials. It can be concluded from energy dispersive X-ray (EDX) mapping (Fig. S1d and S3e†) that C, N, O and Fe are evenly distributed in the catalysts. High-angle annular dark-field scanning transmission electron microscopy (HAADF-STEM) shows no bright dots until using aberration-corrected (AC) HAADF-STEM (Fig. 1c and S3c–f†), further demonstrating that there are only Fe single atom sites in the two catalysts. The valence and coordination environment of Fe atoms in the prepared catalysts were analyzed using synchrotron X-ray absorption spectroscopy (XAS). Fig. 1d shows the Fe K-edge X-ray absorption near edge structure (XANES) spectra of FeN_5 and FeN_6. They exhibited different energy absorption edge profiles, demonstrating that the valence of Fe in FeN_6 is higher than that in FeN_5. The Fourier transformed extended X-ray absorption fine structure (FT-EXAFS) (Fig. 1e) indicates that only one dominate peak around 1.5 Å exists in these materials, which can be attributed to the first Fe–N/O shell.[18] The absence of the Fe–Fe peak around 2.2 Å in the two catalysts further confirms the atomic dispersion of Fe. Furthermore, the fitting results (Fig. S5 and Table S3†) show that the coordination numbers of the two samples are 5.5 and 6, respectively. Moreover, the wavelet transform (WT) of $\chi(k)$ spectra (Fig. S6†) reveals that the centers of the [k, R] intensity maximum for FeN_5 and FeN_6 are similar, while significantly different from that of Fe foil, indicating that only Fe–N/O bonds are present in our samples. X-ray photoelectron spectroscopy (XPS) was used to analyze the non-metallic and metallic elements in detail in the catalyst to exclude oxygen coordination (Table S2†). The spectral profile of N 1s (Fig. 1f and g) exhibited five peaks corresponding to pyridinic N (398.4 eV), Fe–N (399.5 eV), pyrrolic N (400.1 eV), graphitic N (401.0 eV), and oxidized N (403.2 eV).[19,30] The contents of pyrrolic N and pyridinic N significantly decreased in FeN_5 due to hydrogen treatment (Table S4†). In addition, no M–O bond (530 eV) was observed in the O 1s spectrum (Fig. S8†).[25,31] These results confirmed that Fe–N_5 and Fe–N_6 are the actual Fe sites of the two catalysts. The Fe spectral profile (Fig. S9†) indicated that the oxidation state was between +2 and +3, and the content of Fe^{3+} in FeN_6 was higher than that in FeN_5, which are consistent with XANES results (Fig. S7 and Table S5†) and further confirm the higher valence of Fe in FeN_6. In conclusion, mesoporous Fe SACs with high coordination numbers were successfully synthesized. Next, these SACs are used to explore the difference in catalytic performance under different electrolyte conditions.

3.2 CO_2 electrochemical reduction performance

The electrochemical CO_2RR performance was tested in a three-electrode setup using the H-type cell with CO_2 saturated solution (Fig. S10 and Table S6†). Although different electrolyte conditions will lead to pH changes, this change is very small, and the effect of pH on the properties of Fe SACs has been explored by previous researchers,[21] so the effect of pH is no longer considered in this paper. The gas products were quantified by gas chromatography (Fig. S12 and S13†). No other products except CO and H_2 can be detected (Fig. S11†). It is surprising that no clear trends of cation activity on FeN_6 can be observed (Fig. 2a and S15a, b†). Similarly, the FE_{CO} values are close for FeN_5 for different cations, only the case of Na^+ is slightly lower (Fig. S20b†). These contrast with metal catalysts like Ag[16] and Cu,[17] for which the selectivity of the CO_2RR typically increases with increasing cation radius. However, when

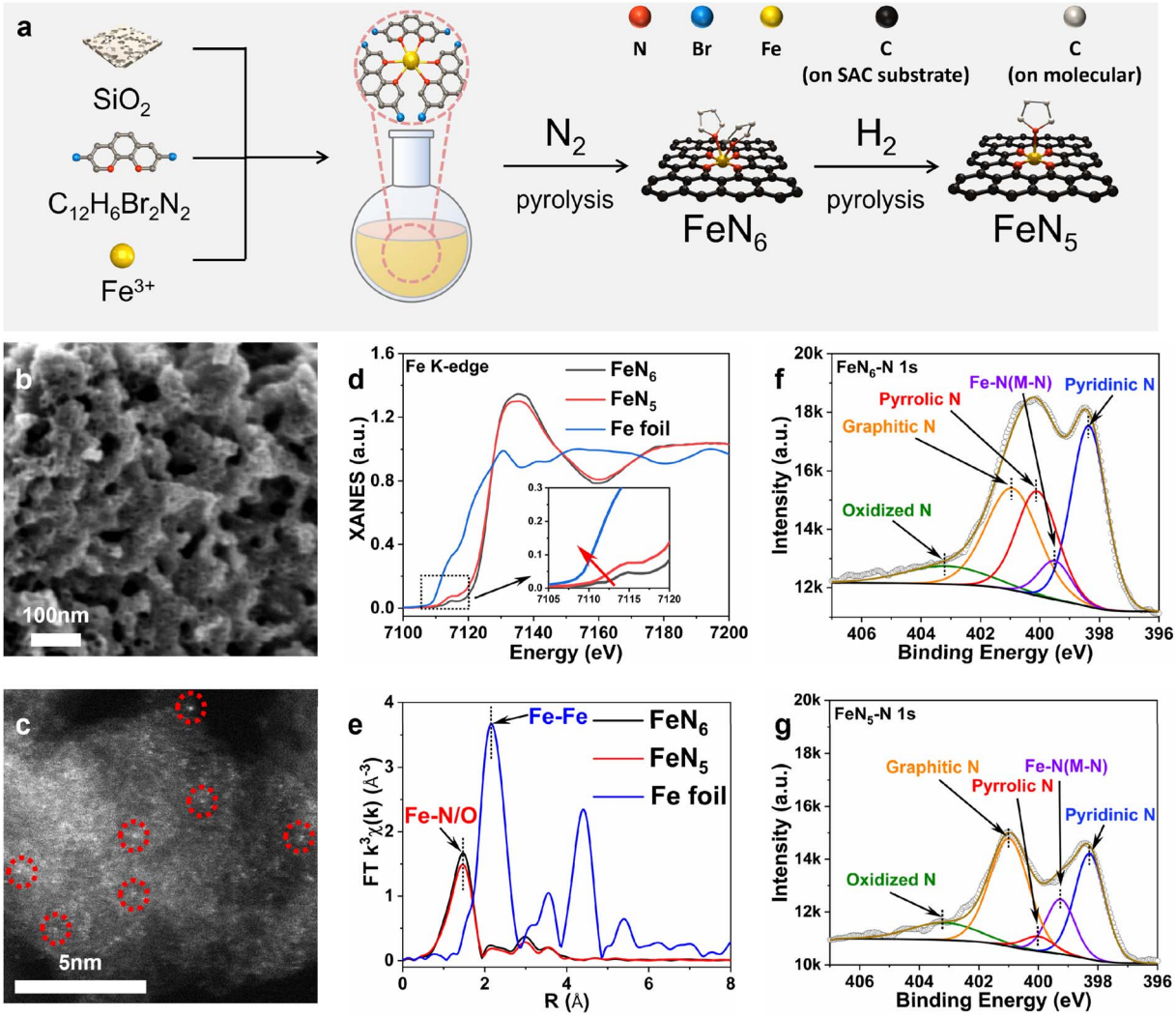

Fig. 1 (a) Schematic illustration of the hard template method for preparing FeN_6 and FeN_5. (b) SEM image of FeN_6. (c) AC-HADDF-STEM image of FeN_6 (red circles are the Fe single atom sites). (d) The Fe K-edge XANES spectra. (e) The Fe K-edge FT-EXAFS spectra. (f) The N spectrum of FeN_6. (g) The N spectrum of FeN_5.

increasing the cation concentration (Fig. 2b, S15c, d and S19b†), it can be found for both FeN_5 and FeN_6 that the FE_{CO} significantly improved at low overpotentials, but decreased at high overpotentials. These observations align with prior studies on SACs,[23,32] indicating that SACs share strong interactions with electrolyte species. As demonstrated in the linear sweep voltammetry (LSV) test (Fig. S16, S19a and S20a†), the activity of the catalysts increases noticeably as the electrolyte concentration increases, and the order of activity follows the sequence: $Rb^+ > K^+ > Na^+$ under all conditions.

To gain a better understanding of the changes in selectivity and activity, the partial CO and H_2 current densities (J_{CO} and J_{H_2}) are examined, which could more accurately reflect the CO_2RR and HER activity. As seen in Fig. $2c_1$ and c_2, J_{CO} and J_{H_2} follow the same order as $Rb^+ > K^+ > Na^+$ (Fig. S17a–c, S18a–c and S20c, d†). This result may explain the reason that no clear trend of FE_{CO} was observed on FeN_6 and FeN_5 with different cations, as the HER is aggravated simultaneously. In addition to cations, it is noteworthy that J_{CO} and J_{H_2} of both SACs (Fig. S17d–f, S18d–f and S19c, d†) were also boosted with increasing cation concentration, except that the J_{CO} of FeN_6 shows a volcano trend at high overpotentials. The enhanced HER is related to the plateau or even the declining trend of J_{CO} at the 0.5 M concentration electrolyte. Therefore, it can be concluded that higher concentration and larger cations can simultaneously promote the CO_2RR and HER on Fe SACs. Such phenomena differ significantly from traditional metal catalysts where only the CO_2RR can be promoted but the HER did not change obviously or even be hindered under the same conditions,[33,34] and thus further investigation is required to explain these unique findings.

To determine whether the alkali metal cation or the bicarbonate is the major factor for the electrolyte effect, we conducted experiments with constant alkali metal cations or bicarbonate concentrations for FeN_6 first. As shown in Fig. $2d_1$ and d_2, changing the Rb^+ concentration significantly affects selectivity and activity. Increasing the Rb^+ concentration promotes J_{CO} at low overpotentials but it reaches a plateau at

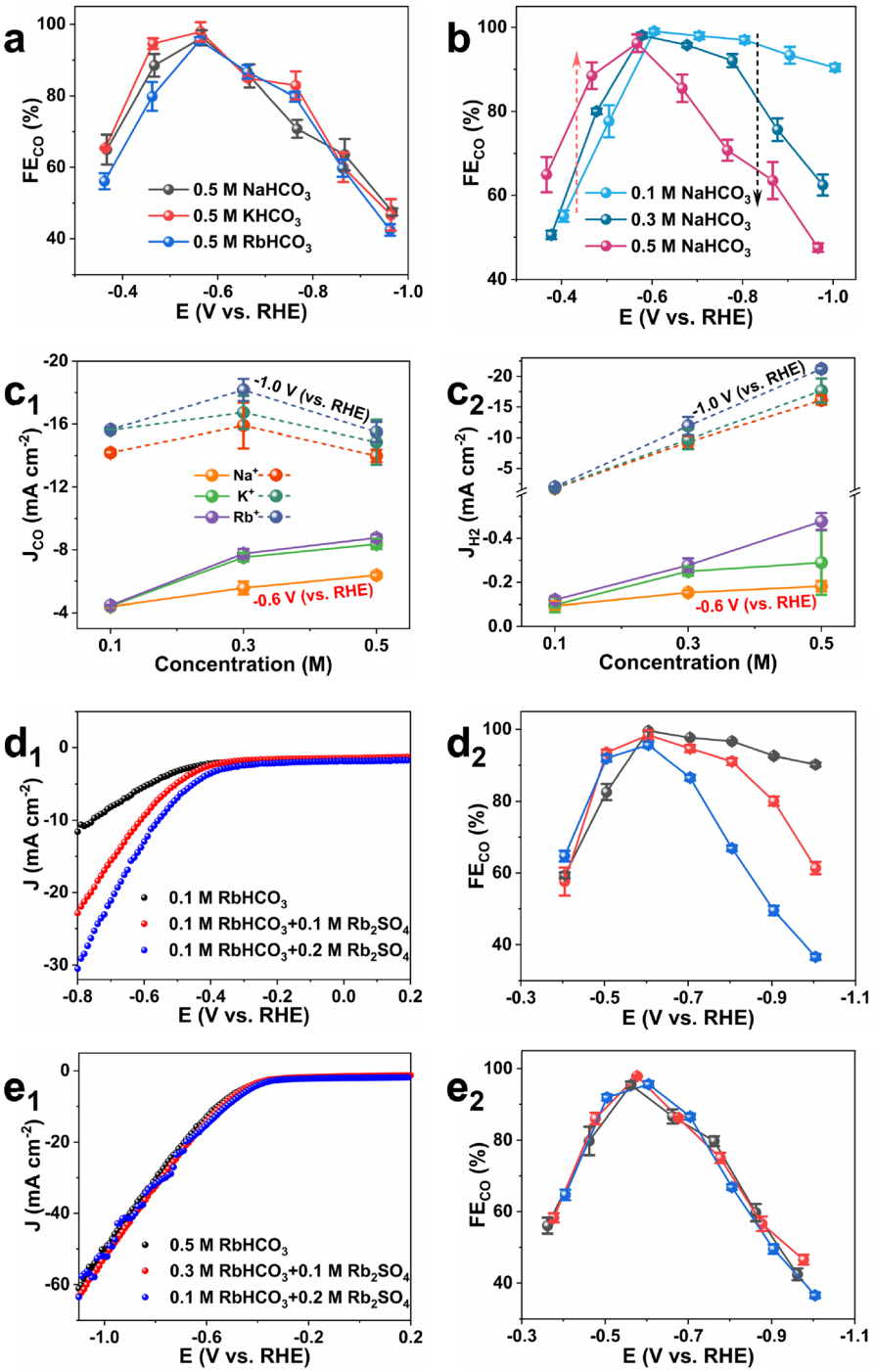

Fig. 2 The FE_{CO} of FeN_6 under the (a) same concentration conditions and (b) same cation conditions. The (c_1) J_{CO} and (c_2) J_{H_2} of FeN_6 at low overpotential (about −0.6 V *vs.* RHE) and high overpotential (about −1.0 V *vs.* RHE) under different electrolyte conditions. The (d_1) LSV and (d_2) FE_{CO} at a constant concentration of HCO_3^-. The (e_1) LSV, (e_2) FE_{CO} at a constant concentration of Rb^+.

high overpotentials (Fig. S26a$_1$ and a$_2$†), while J_{H_2} increases at the whole potential range. This is very similar to the change in $RbHCO_3$ concentration discussed earlier. However, when the concentration of Rb^+ is constant, the catalytic performance has no obvious change (Fig. 2e$_1$, e$_2$ and S26b$_1$, b$_2$†). Similar results were obtained with different alkali metal cations (Na^+ and K^+) and FeN_5 (Fig. S25, S27, S28 and Tables S7–S12†). These experiments reveal that the concentration of alkali metal cations is the primary factor, illustrating the essential role of cations present in the electrolyte in the SAC activity. Moreover, bicarbonate may not affect the performance of SACs because HCO_3^- is negatively charged, making it difficult to access the interface layer and participate in the proton–electron transfer process, which is different from previous results on metal catalysts.[15]

3.3 Identifying the reaction site to uncover the cation influence

In traditional metal catalysts, both the CO_2RR and HER occur at the same site, which means that the competition between the two reactions is essentially a competition for the adsorbed species.[35] However, for SACs with a variety of active sites, the CO_2RR and HER could occur at different sites whiling competing for charges (Fig. 3d). Due to the diversity of catalytically active sites on SACs, we first distinguish the HER and CO_2RR sites through poisoning the Fe single atom sites with SCN^- *via* specific adsorption (Fig. 3a and b).[36] It should be noted that the overall cation concentration is controlled to be constant, this is to prevent the performance change from being caused by cations. The addition of KSCN to the electrolyte indeed inhibited the CO_2RR in both catalysts. However, in an Ar atmosphere where no CO_2RR product was detected (Fig. S24†), the LSV curves corresponding to the HER did not show any significant changes (Fig. 3c). Based on our XPS and XAS results (Fig. 1d–g), it can be concluded that the Fe–N_x sites are the actual CO_2RR site, while the pyridine N and pyrrolic N sites are the HER sites, consistent with previous studies.[18,37] Therefore, the decreased HER activity of FeN_5 compared to FeN_6 under Ar conditions (Fig. 3c and S23†) results from the removal of pyridine N and pyrrolic N by hydrogen treatment. Besides, FeN_5 has higher FE_{CO} and $J_{CO\ ECSA}$ than FeN_6 (Fig. S22†), and previous research[30] reveals that this is due to the more active site FeN_5 than FeN_6, however, in this work, we confirm that the N site can also influence the performance. Therefore, we propose a "trade-off effect" to describe the electrolyte effect on CO_2RR activity for Fe SACs, where the two competing active sites are responsive to cations in the electrolyte. Since previous studies[38,39] have examined the role of alkali metal cations in the HER and revealed their effect on accelerating the Volmer step ($H_2O \rightarrow OH^- + *H$), our focus here is to explore the cation effect on FeN_x sites during the CO_2RR.

3.4 Revealing the bonding interaction between cations and intermediates

To gain mechanistic understanding of the effect of different cations on the CO_2RR catalytic process, DFT simulations were respectively performed on FeN_5 and FeN_6 catalysts. First, we construct two different FeN_5 structural models based on the fine structure analysis shown in Fig. S31a and b.† Table S13† indicates that using pyrrolic N as the coordinating ligand to build FeN_5 based on the planar FeN_4 is more stable than the pyridinic N ligand. In light of this result, we continue to simulate FeN_6 using dual pyrrolic N ligands (Fig. S31c†). The FeN_6 using dual pyridinic N is also created, but this structure cannot exist stably (Fig. S31d†), so it can be confirmed that the two additional N in FeN_6 are pyrrole N. The two pyrrole N are transformed from the pyridine N in the *o*-phenanthroline ring at high temperature. Previous studies have shown that it is unfavourable for CO_2 adsorption when the two pyrrole nitrogen ligands are on opposite sides.[30] Here, we chose to investigate the CO_2RR using pyrrole N ligands positioned on the same side. Additionally, the pyrrolic N and pyridinic N are also created (Fig. S32†) as HER sites. Fig. 4b shows that FeN_5 and FeN_6 have lower $*CO_2$ free energy than *H while the pyrrolic N and pyridinic N

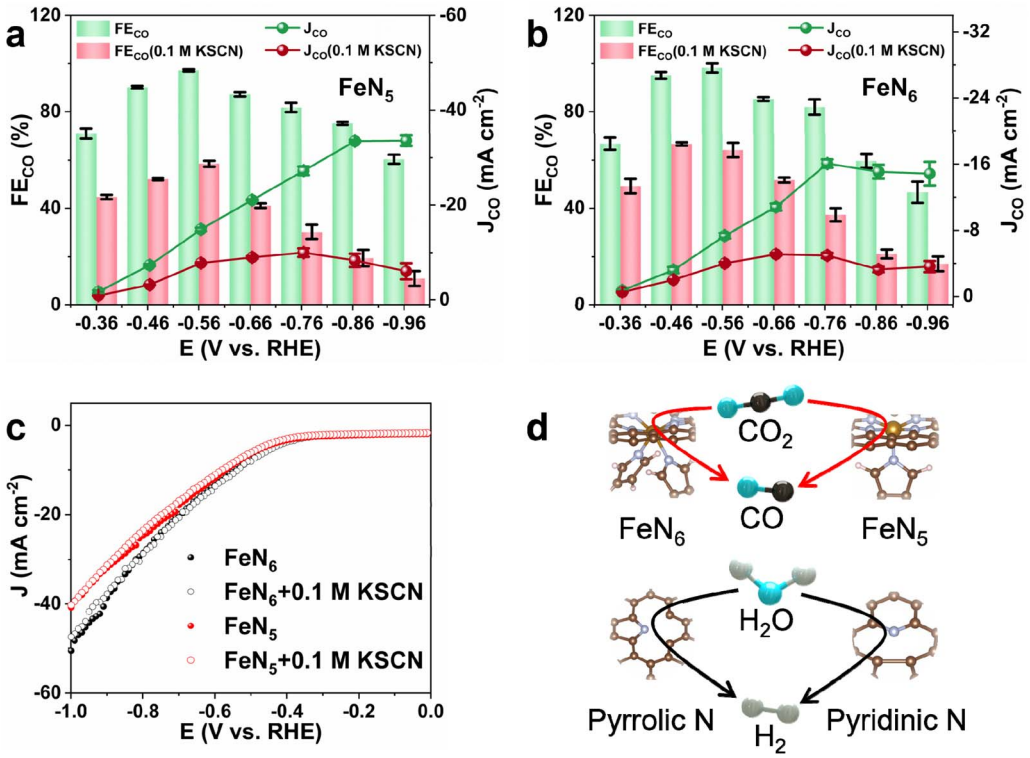

Fig. 3 Catalytic performance of (a) FeN_6 and (b) FeN_5 with (0.4 M $KHCO_3$ + 0.1 M KSCN) and without 0.1 M KSCN (0.5 M $KHCO_3$). (c) The LSV curves of FeN_5 and FeN_6 in an Ar atmosphere with and without 0.1 M KSCN. (d) Schematic illustration of reaction sites in Fe SACs.

are favorable for *H adsorption, supporting that the CO_2RR occurs at the $FeN_{5/6}$ and the pyrrolic N/pyridinic N is more prone to the HER. The free energy comparison further confirms the trade-off effect, where two different functional sites undergo different reactions under negative bias.

Based on the knowledge of previous research on the impact of cations on the CO_2RR, we speculate that the main reason for the influence of cation concentration and species on FeN_x sites is the change in the charge distribution, which causes the adsorption strength of intermediates to change. Because in recent years, researchers have discovered that alkali metal cations can bind with intermediates and stabilize them.[40] We first identify the critical intermediates (*i.e.*, the adsorbed species corresponding to the rate-determining step (RDS)) on different catalysts to accurately describe the influence of alkali metal cations. Fig. S33 and S34† reveal that the adsorption of CO_2 and the formation of *COOH correspond to the RDS of FeN_5 and FeN_6, respectively. Based on these findings, $*CO_2$ and *COOH are designated as the key adsorbed species of FeN_5 and FeN_6 for the study of the cation effect. Additionally, the RDS energy barrier of FeN_5 is lower than that of FeN_6, which further demonstrates its superior catalytic performance (Fig. S34†). To investigate the effect of cations on the FeN_5 and FeN_6 sites and confirm our speculation, DFT-CES simulation was employed, as it allows for precise examination of atomic details at the catalyst–electrolyte interface.[41] Besides, this method can also help us understand how cations affect the adsorption strength of intermediates. The DFT-CES calculation (Fig. 4c and Table S14†) indicates that the adsorption of both $*CO_2$ (on FeN_5) and *COOH (on FeN_6) is enhanced in the presence of cations compared to pure water. This finding suggests that higher cation concentrations can result in better performance, as more cations can reach the inner Helmholtz layer and act on more FeN_x sites to facilitate the CO_2RR.[42] Moreover, cations with

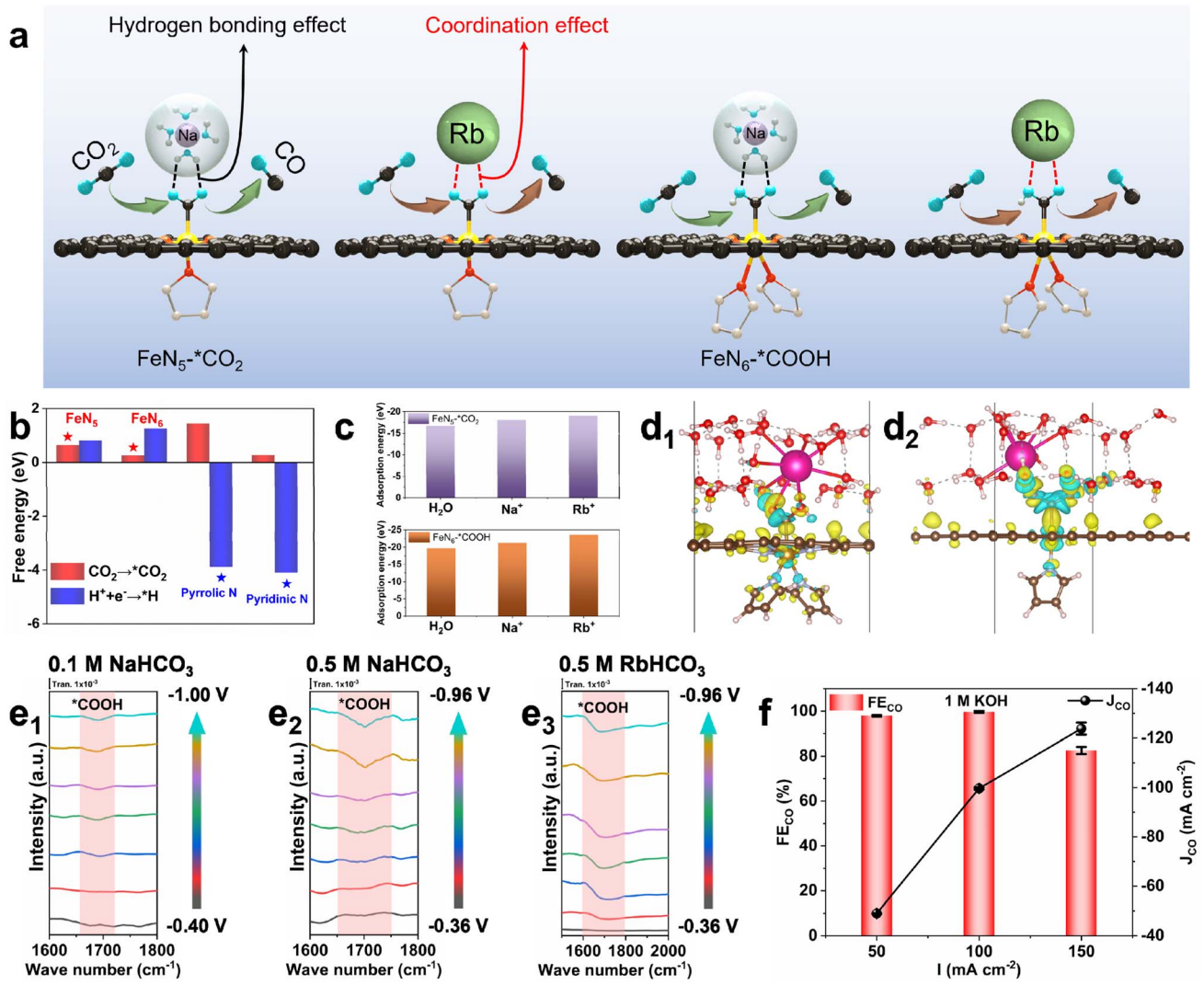

Fig. 4 (a) Schematic illustration of the effect of different cations on reaction sites. The Gibbs free energy of (b) different reactions on different sites and (c) different intermediates under various electrolyte conditions. The charge density difference (CDD) of (d_1) FeN_6 with adsorbed *COOH under Rb^+ conditions and (d_2) FeN_5 with adsorbed $*CO_2$ under Rb^+ conditions. The *in situ* SR-FTIR spectrum of FeN_6 in (e_1) 0.1 M $NaHCO_3$, (e_2) 0.5 M $NaHCO_3$, and (e_3) 0.5 M $RbHCO_3$. (f) The FE_{CO} and J_{CO} of FeN_5 under flow cell conditions (1 M KOH).

larger radii (*e.g.*, Rb^+) can further promote the adsorption of intermediates. The examination of the charge distribution (Fig. 4d and S35–S37†) reveals that cations can enhance the charge transfer by coordination, facilitating charge accumulation in the intermediate and promoting its adsorption. Furthermore, it is important to note that in addition to the direct coordination effect of cations, there is also an indirect effect to facilitate charge transfer. Further analysis of bonding length (Table S15†) reveals that H_2O can also interact with the intermediate. Specifically, the H atom of H_2O bonds with the O atom of $*CO_2$ and *COOH, forming hydrogen bonds that alter the charge distribution. Based on our analysis, the conclusion can be drawn that the cation has two kinds of effects on charge accumulation in the intermediate. First, the cation directly coordinates with the intermediate to facilitate charge transfer. Second, the coordination between the O atom in H_2O and the cation alters the charge distribution in the water molecule. This, in turn, strengthens the hydrogen bond effect between the H atom in H_2O and the O atom in the intermediate. We suspect that the direct bonding of cations has a stronger effect on the promotion of charge transfer than that of the hydrogen bond, which is relatively weak intermolecular interaction. Therefore, the presence of Rb^+ enhances adsorption. This is due to the fact that larger cations have a thinner solvation shell, which enables them to approach the intermediates more closely.[35] As a result, the direct coordination is enhanced. In contrast, Na^+ with a larger solvation shell is predominantly influenced by indirect hydrogen bonding through H_2O, resulting in weaker adsorption than Rb^+. In conclusion, higher concentration and larger cations can facilitate the stabilization of key intermediates at more sites, thus accelerating the CO_2RR (Fig. 4a). To validate the above conclusion, *in situ* SR-FTIR was employed to detect the intermediate. As presented in Fig. 4e_1–e_3, the vibration band at 1700 cm^{-1} can be assigned to the C=O stretching of the generated *COOH intermediate during the CO_2RR.[43] A greater extent of the critical *COOH intermediate on FeN_6 could be observed with larger cations and higher concentration, which is consistent with the DFT-CET calculation results that an increase in charge transfer promotes the adsorption of *COOH. The *in situ* spectroscopy tests confirm that changes in cation species and their concentration could indeed alter the distribution of intermediates on the FeN_x active sites. Based on these findings, we select FeN_5 for CO_2RR tests under flow cell conditions with a high cation concentration (1 M KOH), as it exhibits better catalytic ability and strong alkaline conditions that can inhibit the HER.[22] The reason why RbOH is not selected as the electrolyte is that its price is too expensive, so the cost of configuring it into a high-concentration electrolyte is not appropriate. As shown in Fig. 4f, S38 and S39,† the maximal FE_{CO} can reach approximately 100% at 100 mA cm^{-2}. The impressive CO_2-to-CO performance of FeN_5 highlights its potential for practical applications.

4. Conclusion

In summary, FeN_5 and FeN_6 were first synthesized using a facile hard template method. These catalysts exhibit enhanced performance for both the CO_2RR and HER under higher concentration and larger cation radius conditions, owing to their unique structure. Through rational experiments and DFT simulations, we propose the trade-off effect to explain the unconventional phenomenon, where cations can act on different functional sites of the catalyst. In addition, it was also found that the promotion effect of cations on FeN_5 and FeN_6 is mainly due to the promotion of charge accumulation in $*CO_2$ and *COOH, thereby enhancing the adsorption strength. Cations promote charge transfer through direct coordination and indirect hydrogen bonding. Larger cations can further promote the stabilization of intermediates through direct coordination. This work provides a novel concept for understanding the interaction between alkaline metal cations and Fe SACs and offers valuable insights for future SACs and electrolyte design.

Data availability

The data supporting this article have been included as part of the ESI.†

Author contributions

Yecheng Li: conceptualization, formal analysis, investigation, methodology, visualization, writing – original draft; Songjie Meng: methodology, formal analysis, writing – review & editing; Zihong Wang: investigation, formal analysis, writing – review & editing, supervision; Hehe Zhang: investigation; Xin Zhao: investigation, writing – review & editing, supervision; Qingshun Nian: investigation, writing – review & editing, supervision; Digen Ruan: investigation, supervision; Zhansheng Lu: methodology, formal analysis; Xiaodi Ren: conceptualization, funding acquisition, methodology, supervision, writing – review & editing.

Conflicts of interest

The authors declare no competing financial interest.

Acknowledgements

This study was supported by the National Natural Science Foundation of China (Grant No. 22179124, 21905265, and 12274118), the Fundamental Research Funds for the Central Universities (WK3430000007), and Henan Center for Outstanding Overseas Scientists (No. GZS2023007). The SR-FTIR was performed at the Infrared Spectroscopy and Microspectroscopy Endstation (BL01B) in the National Synchrotron Radiation Laboratory (NSRL) in Hefei, China; the DFT simulation was supported by the High Performance Computing Center of Henan Normal University.

References

1 J. Li, H. Zeng, X. Dong, Y. Ding, S. Hu, R. Zhang, Y. Dai, P. Cui, Z. Xiao, D. Zhao, L. Zhou, T. Zheng, J. Xiao, J. Zeng and C. Xia, *Nat. Commun.*, 2023, **14**, 340.

2 H. Guo, D.-H. Si, H.-J. Zhu, Q.-X. Li, Y.-B. Huang and R. Cao, *eScience*, 2022, **2**, 295–303.
3 L. Li, Z. Liu, X. Yu and M. Zhong, *Angew Chem. Int. Ed. Engl.*, 2023, **135**, e202300226.
4 Z. Tao, Z. Wu, X. Yuan, Y. Wu and H. Wang, *ACS Catal.*, 2019, **9**, 10894–10898.
5 J. Zhao, P. Zhang, T. Yuan, D. Cheng, S. Zhen, H. Gao, T. Wang, Z. J. Zhao and J. Gong, *J. Am. Chem. Soc.*, 2023, **145**, 6622–6627.
6 X. Tan, K. Sun, Z. Zhuang, B. Hu, Y. Zhang, Q. Liu, C. He, Z. Xu, C. Chen, H. Xiao and C. Chen, *J. Am. Chem. Soc.*, 2023, **145**, 8656–8664.
7 Z. Wang, Y. Li, X. Zhao, S. Chen, Q. Nian, X. Luo, J. Fan, D. Ruan, B. Q. Xiong and X. Ren, *J. Am. Chem. Soc.*, 2023, **145**, 6339–6348.
8 D. Xiao, X. Bao, M. Zhang, Z. Li, Z. Wang, Y. Gao, Z. Zheng, P. Wang, H. Cheng, Y. Liu, Y. Dai and B. Huang, *Chem. Eng. J.*, 2023, **452**, 139358.
9 W. Li, Z. Yin, Z. Gao, G. Wang, Z. Li, F. Wei, X. Wei, H. Peng, X. Hu, L. Xiao, J. Lu and L. Zhuang, *Nat. Energy*, 2022, **7**, 835–843.
10 A. Xu, S.-F. Hung, A. Cao, Z. Wang, N. Karmodak, J. E. Huang, Y. Yan, A. Sedighian Rasouli, A. Ozden, F.-Y. Wu, Z.-Y. Lin, H.-J. Tsai, T.-J. Lee, F. Li, M. Luo, Y. Wang, X. Wang, J. Abed, Z. Wang, D.-H. Nam, Y. C. Li, A. H. Ip, D. Sinton, C. Dong and E. H. Sargent, *Nat. Catal.*, 2022, **5**, 1081–1088.
11 S. Kuang, Y. Su, M. Li, H. Liu, H. Chuai, X. Chen, E. J. M. Hensen, T. J. Meyer, S. Zhang and X. Ma, *Proc. Natl. Acad. Sci. U. S. A.*, 2023, **120**, e2214175120.
12 Y. N. Gong, C. Y. Cao, W. J. Shi, J. H. Zhang, J. H. Deng, T. B. Lu and D. C. Zhong, *Angew Chem. Int. Ed. Engl.*, 2022, **61**, e202215187.
13 J. Yin, J. Jin, Z. Yin, L. Zhu, X. Du, Y. Peng, P. Xi, C. H. Yan and S. Sun, *Nat. Commun.*, 2023, **14**, 1724.
14 Z.-M. Zhang, T. Wang, Y.-C. Cai, X.-Y. Li, J.-Y. Ye, Y. Zhou, N. Tian, Z.-Y. Zhou and S.-G. Sun, *Nat. Catal.*, 2024, **7**, 807–817.
15 G. Marcandalli, A. Goyal and M. T. M. Koper, *ACS Catal.*, 2021, **11**, 4936–4945.
16 M. R. Singh, Y. Kwon, Y. Lum, J. W. Ager and A. T. Bell, *J. Am. Chem. Soc.*, 2016, **138**, 13006–13012.
17 J. Resasco, L. D. Chen, E. Clark, C. Tsai, C. Hahn, T. F. Jaramillo, K. Chan and A. T. Bell, *J. Am. Chem. Soc.*, 2017, **139**, 11277–11287.
18 C. Liu, Y. Wu, K. Sun, J. Fang, A. Huang, Y. Pan, W.-C. Cheong, Z. Zhuang, Z. Zhuang, Q. Yuan, H. L. Xin, C. Zhang, J. Zhang, H. Xiao, C. Chen and Y. Li, *Chem*, 2021, **7**, 1297–1307.
19 Y. Wang, B. J. Park, V. K. Paidi, R. Huang, Y. Lee, K.-J. Noh, K.-S. Lee and J. W. Han, *ACS Energy Lett.*, 2022, **7**, 640–649.
20 S. Chen, X. Li, C. W. Kao, T. Luo, K. Chen, J. Fu, C. Ma, H. Li, M. Li, T. S. Chan and M. Liu, *Angew Chem. Int. Ed. Engl.*, 2022, **61**, e202206233.
21 J. Gu, C.-S. Hsu, L. Bai, H. M. Chen and X. Hu, *Science*, 2019, **364**, 1091–1094.
22 A. S. Varela, M. Kroschel, N. D. Leonard, W. Ju, J. Steinberg, A. Bagger, J. Rossmeisl and P. Strasser, *ACS Energy Lett.*, 2018, **3**, 812–817.
23 F. Pan, B. Li, E. Sarnello, S. Hwang, Y. Gang, X. Feng, X. Xiang, N. M. Adli, T. Li, D. Su, G. Wu, G. Wang and Y. Li, *Nano Energy*, 2020, **68**, 104384.
24 H. Zhang, J. Li, S. Xi, Y. Du, X. Hai, J. Wang, H. Xu, G. Wu, J. Zhang, J. Lu and J. Wang, *Angew Chem. Int. Ed. Engl.*, 2019, **58**, 14871–14876.
25 T. Zhang, X. Han, H. Liu, M. Biset-Peiró, J. Li, X. Zhang, P. Tang, B. Yang, L. Zheng, J. R. Morante and J. Arbiol, *Adv. Funct. Mater.*, 2022, **32**, 2111446.
26 D. R. Hamann, M. Schlüter and C. Chiang, *Phys. Rev. Lett.*, 1979, **43**, 1494–1497.
27 J. P. Perdew, K. Burke and M. Ernzerhof, *Phys. Rev. Lett.*, 1996, **77**, 3865–3868.
28 T. Sheng and S.-G. Sun, *Chem. Phys. Lett.*, 2017, **688**, 37–42.
29 X. Qin, T. Vegge and H. A. Hansen, *J. Am. Chem. Soc.*, 2023, **145**, 1897–1905.
30 H. Chen, X. Guo, X. Kong, Y. Xing, Y. Liu, B. Yu, Q.-X. Li, Z. Geng, R. Si and J. Zeng, *Green Chem.*, 2020, **22**, 7529–7536.
31 S. Huang, B. Hu, S. Zhao, S. Zhang, M. Wang, Q. Jia, L. He, Z. Zhang and M. Du, *Chem. Eng. J.*, 2022, **430**, 132933.
32 H. Cheng, X. Wu, X. Li, X. Nie, S. Fan, M. Feng, Z. Fan, M. Tan, Y. Chen and G. He, *Chem. Eng. J.*, 2021, **407**, 126842.
33 W. Ren, A. Xu, K. Chan and X. Hu, *Angew Chem. Int. Ed. Engl.*, 2022, **61**, e202214173.
34 A. S. Malkani, J. Anibal and B. Xu, *ACS Catal.*, 2020, **10**, 14871–14876.
35 B. Pan, Y. Wang and Y. Li, *Chem Catal.*, 2022, **2**, 1267–1276.
36 Y. Chen, L. Zou, H. Liu, C. Chen, Q. Wang, M. Gu, B. Yang, Z. Zou, J. Fang and H. Yang, *J. Phys. Chem. C*, 2019, **123**, 16651–16659.
37 C. Wang, Y. Liu, H. Ren, Q. Guan, S. Chou and W. Li, *ACS Catal.*, 2022, **12**, 2513–2521.
38 M. C. O. Monteiro, A. Goyal, P. Moerland and M. T. M. Koper, *ACS Catal.*, 2021, **11**, 14328–14335.
39 J. T. Bender, A. S. Petersen, F. C. Østergaard, M. A. Wood, S. M. J. Heffernan, D. J. Milliron, J. Rossmeisl and J. Resasco, *ACS Energy Lett.*, 2022, **8**, 657–665.
40 M. C. O. Monteiro, F. Dattila, B. Hagedoorn, R. García-Muelas, N. López and M. T. M. Koper, *Nat. Catal.*, 2021, **4**, 654–662.
41 S. J. Shin, H. Choi, S. Ringe, D. H. Won, H. S. Oh, D. H. Kim, T. Lee, D. H. Nam, H. Kim and C. H. Choi, *Nat. Commun.*, 2022, **13**, 5482.
42 J. Yu, J. Yin, R. Li, Y. Ma and Z. Fan, *Chem Catal.*, 2022, **2**, 2229–2252.
43 J. Pei, T. Wang, R. Sui, X. Zhang, D. Zhou, F. Qin, X. Zhao, Q. Liu, W. Yan, J. Dong, L. Zheng, A. Li, J. Mao, W. Zhu, W. Chen and Z. Zhuang, *Energy Environ. Sci.*, 2021, **14**, 3019–3028.